Numerical Models' Effect in Asymmetrical Flow Driving in Tow-Sided Lid-Driven Cavity

El Amin AZZOUZ[*†a], Samir HOUAT[b]

a. Université Mohamed Ben Ahmed Oran 2, Institut de Maintenance et de Sécurité Industrielle, IMSI, Oran, Algérie
E-mail : aminazouz31@yahoo.com
b. Laboratoire de modélisation numérique et expérimentale de phénomènes mécaniques, MNEPM, Université de Mostaganem, Mostaganem, Algérie
E-mail : samir.houat@univ-mosta.dz

Abstract:

steady two-dimensional flow in driven cavities is often handled numerically with the laminar model even at relatively high Reynolds numbers. The onset of turbulent flow still surrounded by some ambiguities concerning the appearance of the first Hopf bifurcation. Under the light of these facts, the present paper mainly aims to numerically illustrate the difference effectiveness of the Spalart-Allmaras (SA), the Renormalization Group K-epsilon (RNG K-ε), the Shear Stress Transport K-omega (SST K-ω), and the Reynolds stress (RSM) turbulence models (RANS turbulence models) against the laminar model. The problem under examination is represented by a two-dimensional flow in two-sided lid-driven square cavity. The top and bottom walls slide in opposite direction (antiparallel wall motion) with different velocities related to two various velocity ratios λ=-7 and -10. The predicted numerical results are computed with the Finite Volume method (FVM) based on the second scheme of accuracy. From the examination of the computational results, it is seen that the SST K-ω model, the Stress-omega Reynolds stress model (Omega RSM), and the laminar model shows a high efficiency compared to the salient weakened for the Spalart-Allmaras (SA) model, the RNG K-ε model, and the Linear pressure strain Reynolds stress model (LPS-RSM) near end walls. However, the laminar model outperforms all of RANS turbulence models when λ=-10. As a result, we believe that the laminar model is numerically the most convenient model for two-dimensional driven cavities problems at relatively high Reynolds numbers until a solution ceases to converge.

Keywords: Two-sided; Lid-driven cavity; Antiparallel wall motion; Asymmetrical driving; Laminar model; RANS models

1 Introduction

Two-sided lid-driven cavity problem has been considered a good benchmarking example following the conventional one-sided lid-driven cavity. The type of flow bear similarities to a lot of engineering applications including coating and mixing technologies, flow over cutouts, and chemical etching of film cooling. The first experimental and numerical investigations of the flow are due to [1-3] in order to

investigate two- and three-dimensional flow, instability process, and solutions multiplicity in a two-sided lid-driven cavity.

A set of numerical simulation has been also conducted by [4-12] in order to examine two-dimensional steady flow in a two-sided lid-driven cavity with various aspect ratios either in parallel or antiparallel wall motion. For the same imposed velocity of the two facing wall (symmetrical driving), researchers have been employed a variety of efficient numerical code based on the laminar model even at a relatively high Reynolds number. Basically, they found that the predicted flow structures inside the cavity show a great resemblance among all documented studies especially vortices near end walls when the Reynolds number goes up for a maximum value of Re= 8500.

For different imposed wall velocity (asymmetrical driving), Che Sidik and Razali [13] employed the Lattice Boltzmann Method (LBM) to explore the fluid flow which is driven by two parallel moving walls in a square cavity with different speed ratios varies from 0 to 1, and Reynolds number ranges from 100 to 1000.

The basic idea presented in this paper was inspired by a large number of publications involve the traditional one-sided lid-driven cavity flow studies. Truthfully, they show a discrepancy about the onset of turbulent flow in other words the transition of the flow from the steady state to unsteady state, namely, hydrodynamic stability analysis (presented the appearing of the first Hopf bifurcation in the flow) [14, 15] and Direct numerical simulation (DNS) (presented the transition Reynolds number) [16, 17]. undoubtedly, if the flow is really chaotic and the signs of turbulence stats to appear then one should say that a turbulent model is a required intuitive.

However, the threshold of the onset of the flow unsteadiness was found by [18] within $10500 \leq Re \leq 11000$ for symmetrical driving flow in a two-dimensional two-sided lid-driven square cavity with parallel wall motion, to our best knowledge, there is no published data on this case employed the Reynolds-Averaged Navier-Stokes (RANS) equations in conjunction with a turbulence model on the one hand and the investigation of asymmetrical flow driving in antiparallel wall motion on the other. accordingly, the present paper aims to numerically investigate two-dimensional steady flow in a two-sided lid-driven square cavity when the two facing wall are induced in antiparallel wall motion with different velocity (asymmetrical driving). The main purpose is to benchmark the accuracy and efficiency of the Spalart-Allmaras (SA), the Renormalization Group K-epsilon (RNG K-ε), the Shear Stress Transport K-omega (SST K-ω), and the Reynolds stress (RSM) turbulence models (RANS turbulence models) considering the flow is turbulent against the laminar model assuming the flow is laminar.

According to the obtained results for two velocity ratios λ=-7 and -10, it is observed that the laminar model is numerically the most suitable model to treat two-dimensional driven cavity problem even at relatively high Reynolds numbers. It is worth mentioning that scenarios for three-dimensional flow are quite different were signs of turbulence appear early even with a relatively low Reynolds number.

2 Problem statement

Figure 1 shows the details of the problem under consideration. A two-dimensional two-sided facing lid-driven square cavity filled with a fluid set into motion. The top wall moves in the right direction with different velocities, $U_T = \lambda U_B$, involving a variable velocity ratio, $\lambda = U_T / U_B$. the bottom wall moves to the left direction with a constant velocity U_B obtained through Reynolds number equal to 1000. The two remaining vertical walls are taken to be at rest. Such driving is called antiparallel wall motion with different applied velocities ($Re_1 \neq -Re_2$). Note that no-slip condition at the non-porous walls yields that stream-function value (ψ) vanishes at all boundaries.

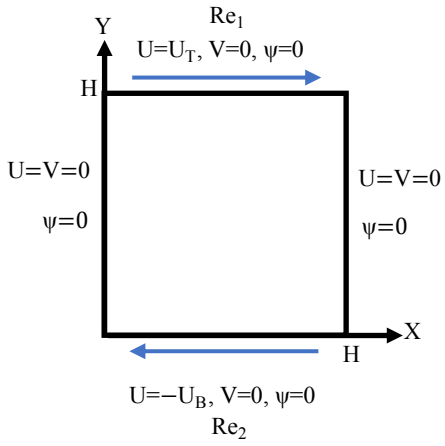

Figure 1 schematic geometry of the cavity and boundary conditions.

3 Mathematical models

Macroscopic flows encountered in the natural world and in engineering practice are either laminar or turbulent. The laminar motion of a fluid in a driven cavity is described by conservation laws of physics (mass and momentum) called Navier-Stokes equations. The whole spectrum of scales is resolved directly and no modelling is required. However, turbulent flow involves fluctuations that are unpredictable. The idea behind using turbulent models is to model the additional unknowns, namely, Reynolds stresses tensors that are introduced by the averaging process in order to close the system of Reynolds averaged Navier-Stokes equations (RANS equations). additionally, the closure procedure presented herein has been carried out either through the Eddy viscosity models (SA, RNG K-ε, and SST K-ω) based on Boussinesq [19] hypothesis with low computational cost or through the Reynolds-Stress Models (RSM) based on the transport equations for Reynolds stresses with more expensive cost. The governing models' equations employed in the present paper will be described briefly were further detail can be found in the literature.

3.1 Laminar model

The fluid employed in this investigation is assumed incompressible and Newtonian. Equations of mass and momentum can be written in the cartesian coordinates for laminar and two-dimensional flow as follow:

- Continuity:

$$\frac{\partial U}{\partial X}+\frac{\partial V}{\partial Y}=0 \tag{1}$$

- Momentum:

$$\rho\frac{\partial(U^2)}{\partial X}+\rho\frac{\partial(UV)}{\partial Y}=\mu\left[\frac{\partial^2 U}{\partial X^2}+\frac{\partial^2 V}{\partial Y^2}\right]-\frac{\partial P}{\partial X} \tag{2}$$

$$\rho\frac{\partial(UV)}{\partial X}+\rho\frac{\partial(V^2)}{\partial Y}=\mu\left[\frac{\partial^2 U}{\partial X^2}+\frac{\partial^2 V}{\partial Y^2}\right]-\frac{\partial P}{\partial Y} \tag{3}$$

Where U, V, P, ρ, and μ represent dimensionless variables of fluid velocities components, pression, fluid density, and dynamic viscosity, respectively. The Reynolds number can be written as:

$$Re_{1,2} = \frac{\rho\, U_{T,B}\, H}{\mu} \tag{4}$$

Where H denotes the physical size of the cavity. Velocity components could be obtained in terms of stream-function (ψ) by:

$$U = -\frac{\partial \psi}{\partial Y}, \qquad V = \frac{\partial \psi}{\partial X} \tag{5}$$

3.2 RANS turbulent models

3.2.1 Spalart-Allmaras model

The proposed one equation model by Spalart-Allmaras [20] solves the transport equation for a modified quantity form of the turbulent Kinematic viscosity, $\tilde{\upsilon}$, with a difference limited only to the near-wall (viscous affected) region with ease in the computation process. It is mainly intended for aerospace applications involving wall-bounded flows, turbomachinery applications, and has shown good results to predict boundary layers flows. the transport equation for $\tilde{\upsilon}$ is given by:

$$\frac{\partial}{\partial t}(\rho\tilde{\upsilon}) + \frac{\partial}{\partial x_i}(\rho\tilde{\upsilon}u_i) = G_\upsilon + \frac{1}{\sigma_{\tilde{\upsilon}}}\left[\frac{\partial}{\partial x_i}\left\{(\mu + \rho\tilde{\upsilon})\frac{\partial \tilde{\upsilon}}{\partial x_j}\right\} + C_{b2}\rho\left(\frac{\partial \tilde{\upsilon}}{\partial x_j}\right)^2\right] - Y_\upsilon + S_{\tilde{\upsilon}} \tag{6}$$

where G_υ and Y_υ denote respectively the production of turbulent viscosity and the destruction of turbulent viscosity that occurs in the near-wall region due to wall blocking and viscous damping. $\sigma_{\tilde{\upsilon}}$ and C_{b2} are constant and υ is the molecular kinematic viscosity. $S_{\tilde{\upsilon}}$ represent a user-defined source term. the modified turbulent Kinematic viscosity, $\tilde{\upsilon}$, vanishes at all boundaries. Note that the Spalart-Allmaras turbulent production is set on vorticity-based.
The turbulent eddy-viscosity is given by:

$$\mu_t = \rho\tilde{\upsilon} f_{\upsilon 1} \tag{7}$$

where the viscous damping function, $f_{\upsilon 1}$, is given by:

$$f_{\upsilon 1} = \frac{(\tilde{\upsilon}/\upsilon)^3}{(\tilde{\upsilon}/\upsilon)^3 + C_{\upsilon 1}^3} \tag{8}$$

3.2.2 Renormalization Group (RNG) K-epsilon model

The RNG K-ε model [21] is considered among the most widely used two-equation models. It represents a modification of the classical standard K-ε model improved by a rigorous statistical technique (renormalization group theory) with better accuracy and reliability in predicting the recirculation length

in separating flows, strained flows, and swirling flows. RNG K-ε model is specified by two transport equations for two turbulence properties as follow:
The turbulence kinetic energy (K) and its dissipation rate (ε) are obtained from:

$$\frac{\partial}{\partial t}(\rho k) + \frac{\partial}{\partial x_i}(\rho k u_i) = \frac{\partial}{\partial x_j}\left(\alpha_k \mu_{eff} \frac{\partial k}{\partial x_j}\right) + G_k + G_b - \rho\varepsilon - Y_M + S_k \quad (9)$$

And

$$\frac{\partial}{\partial t}(\rho \varepsilon) + \frac{\partial}{\partial x_i}(\rho \varepsilon u_i) = \frac{\partial}{\partial x_j}\left(\alpha_\varepsilon \mu_{eff} \frac{\partial \varepsilon}{\partial x_j}\right) + C_{1\varepsilon}\frac{\varepsilon}{k}(G_k + C_{3\varepsilon}G_b) - C_{2\varepsilon}\rho\frac{\varepsilon^2}{k} - R_\varepsilon + S_\varepsilon \quad (10)$$

Where G_k is the generation of turbulent Kinetic energy due to the mean velocity gradients. G_b is the generation of turbulent kinetic energy due to buoyancy. Y_M represents the contribution of the fluctuating dilatation in compressible turbulence. $\alpha_k$and α_ε are the inverse effective Prandtl numbers for k and ε, respectively. S_k and S_ε represent user-defined source terms.
A modified form of the turbulent viscosity μ_t is provided by RNG K- ε model when the mean flow is affected by an important rate of rotation and swirl. The modification form can be expressed by:

$$\mu_t = \mu_{t0} f\left(\alpha_s, \Omega, \frac{k}{\varepsilon}\right) \quad (11)$$

Where μ_{t0} is the value of turbulent viscosity calculated without the swirl modification. Ω is a characteristic swirl number, and α_s is a swirl constant that assumes different values depending on whether the flow is swirl-dominated or only mildly swirling. Note that in the present investigation the near-walls are modelled with the enhanced wall treatment.

3.2.3 The Shear Stress Transport (SST) K-omega model

A more successful Shear Stress Transport (SST) K-ω two-equation turbulence model was developed by Menter [22]. It achieves higher accuracy and reliability for predicting aerodynamics flows, boundary layer with an adverse pressure gradient, zero pressure gradient, and free shear layer. This is due to the effective combination of the k- ω model in the near-wall region and the free-stream independence of the k-ε model in the far field zones. The turbulence kinetic energy (K) and the specific dissipation rate (ω) are obtained from the following transport equations:

$$\frac{\partial}{\partial t}(\rho k) + \frac{\partial}{\partial x_i}(\rho k u_i) = \frac{\partial}{\partial x_j}\left(\Gamma_k \frac{\partial k}{\partial x_j}\right) + G_k - Y_k + S_k \quad (12)$$

And

$$\frac{\partial}{\partial t}(\rho \omega) + \frac{\partial}{\partial x_i}(\rho \omega u_i) = \frac{\partial}{\partial x_j}\left(\Gamma_\omega \frac{\partial \omega}{\partial x_j}\right) + G_\omega - Y_\omega + D_\omega + S_\omega \quad (13)$$

Where G_k is the generation of turbulent Kinetic energy due to the mean velocity gradients. G_ω is the generation of ω. Γ_k and Γ_ω represent the effective diffusivity of K and ω, respectively. Y_k and Y_ω represent the dissipation of K and ω due to turbulence. D_ω represent the cross-diffusion term. S_k and S_ω are user-defined source terms.
The advantage performance of the SST K- ω model lies on the modified form of the turbulent viscosity $\mu_t$which is expressed as follow:

$$\mu_t = \frac{\rho k}{\omega} \frac{1}{\max\left[\frac{1}{\alpha^*}, \frac{\Omega F_2}{a_1 \omega}\right]} \tag{14}$$

Where

$$\Omega = \sqrt{2\Omega_{ij}\Omega_{ij}} \tag{15}$$

Ω_{ij} is the mean rate of rotation tensor ($\Omega_{ij} = \frac{1}{2}\left(\frac{\partial u_i}{\partial x_j} - \frac{\partial u_j}{\partial x_i}\right)$). α^* is the coefficient damping of the turbulent viscosity ($\alpha^* = \alpha_\infty^* \left(\frac{\alpha_0^* + Re_t/R_k}{1 + Re_t/R_k}\right)$.

The blending functions $F_1$and F_2 which ensure that the model achieves high efficiency in both the near-wall and far from the wall are given by:

$$F_1 = tanh(\Phi_1^4) \tag{16}$$

$$\Phi_1 = \min\left[max\left(\frac{\sqrt{k}}{0.09\omega y}, \frac{500\mu}{\rho y^2 \omega}\right), \frac{4\rho k}{\sigma_{\omega,2} D_\omega^+ y^2}\right] \tag{17}$$

$$D_\omega^+ = max\left[2\rho \frac{1}{\sigma_{\omega,2}} \frac{1}{\omega} \frac{\partial k}{\partial x_j} \frac{\partial \omega}{\partial x_j}, 10^{-20}\right] \tag{18}$$

$$F_2 = tanh(\Phi_2^2) \tag{19}$$

$$\Phi_1 = max\left[2\frac{\sqrt{k}}{0.09\omega y}, \frac{500\mu}{\rho y^2 \omega}\right] \tag{20}$$

where *y* is the distance to the next surface and D_ω^+ is the positive portion of the cross-diffusion term.

3.2.4 The Reynolds stress model

Avoiding the Boussinesq hypothesis (isotropic viscosity assumption) [23-25], the Reynolds Stress Model (RSM) is physically the most attractive, thoughtful, and expensive turbulence model. The Reynolds Averaged Navier-Stokes equations (RANS) are closed by solving the transport equations for the Reynolds stresses that requires more modelling than the one- and two-equation turbulent models. It is very suitable and potential mainly to predict complex 3-D flows, cyclones, swirl combustors, rotating flow passages, and in curved ducts. The partial differential equation (transport equation) for the stress tensor is derived from the Navier-Stokes equation, and can be written as the following form:

$$\underbrace{\frac{\partial}{\partial t}\left(\rho\overline{u_i'u_j'}\right)}_{\substack{\text{local time}\\ \text{derrivative}}} + \underbrace{\frac{\partial}{\partial x_k}\left(\rho u_k \overline{u_i'u_j'}\right)}_{C_{ij}} = \underbrace{-\frac{\partial}{\partial x_k}\left[\rho\overline{u_i'u_j'u_k'} + \overline{p\left(\delta_{kj}u_i' + \delta_{ik}u_j'\right)}\right]}_{D_{T,ij}} + \underbrace{\frac{\partial}{\partial x_k}\left[\mu\frac{\partial}{\partial x_k}\left(\overline{u_i'u_j'}\right)\right]}_{DL_{ij}} \underbrace{-\rho\left(\overline{u_i'u_k'}\frac{\partial u_j}{\partial x_k} + \overline{u_j'u_k'}\frac{\partial u_i}{\partial x_k}\right)}_{P_{ij}}$$

$$\underbrace{-\rho\beta\left(g_i\overline{u_j'\theta} + g_j\overline{u_i'\theta}\right)}_{G_{ij}} + \underbrace{p\left(\overline{\frac{\partial u_i'}{\partial x_j}} + \overline{\frac{\partial u_j'}{\partial x_i}}\right)}_{\phi_{ij}} \underbrace{-2\mu\overline{\frac{\partial u_i'}{\partial x_k}\frac{\partial u_j'}{\partial x_k}}}_{\varepsilon_{ij}} \underbrace{-2\rho\Omega_k\left(\overline{u_j'u_m'}e_{ikm} + \overline{u_i'u_m'}e_{jkm}\right)}_{F_{ij}} \tag{21}$$

C_{ij} represent the convection term, $D_{T,ij}$ is the turbulent diffusion term, DL_{ij} being the molecular diffusion term, P_{ij} is the stress production term, G_{ij} denotes the buoyancy production term, ϕ_{ij} is the pressure strain term, ε_{ij} is the dissipation term, F_{ij} represent the production by system rotation term.
Two turbulence model approaches are presented here to handle the pressure-strain term, ϕ_{ij}, presented in the aforementioned RSM transport equation. The first is the Linear Pressure-Strain (LPS) [23, 26] treated with the Standard Wall Functions for the near-wall treatment. The second is the Stress-Omega model proposed by [27] where no treatment of the wall reflections is required. the Stress-Omega model is based on the omega equations and LLR model. Mostly, it bears a great resemblance to the K-ω model and reveals a great prediction for a wide range of turbulent flows.

4. Solution method

The commercial CFD software package ANSYS FLUENT Vers.16.2 has been applied for the detailed comparative analysis. The code uses a finite volume method [28] based on the second scheme of accuracy to solve the transport equations for both laminar and turbulent models. The coupled algorithm [29] is employed to handle the pressure-velocity coupling ensured more robust results and enabling the control of stability and convergence behaviour. The convergence criteria adopted in this paper was based on a maximum residual of RES= 10^{-8} as a measure of confirmation the convergence to the steady state with very accurate solutions. after performing a comprehensive grid independence study for the one-sided lid-driven cavity (Re_1=1000, Re_2=0), a 257×257 structured hexahedral mesh of non-uniform grid points distributed in a non-equal manner with a higher concentration in the vicinity of the wall is adopted and used for all calculations as shown in Figure 2.

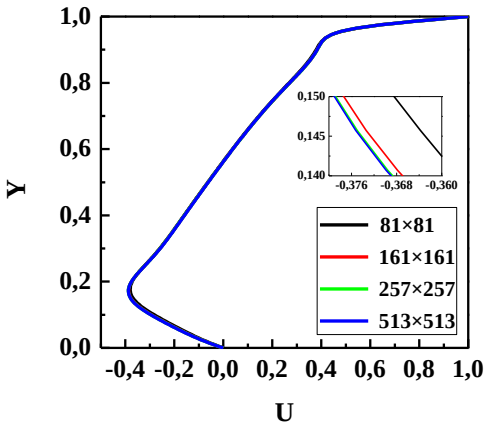

Figure 2 Grid-independence test, U-velocity components passing through the vertical centerline for Re_1=1000 and various mesh resolution.

5. Code validation

In order to confirm the proposed solution method, laminar results of the popular one-sided lid-driven cavity with unit aspect ratio are considered for the validation purpose. Figure 3 shows a comparison of U-components velocity at the vertical centerline of the cavity with the obtained results by Ghia et al [30] on a coarse grid of 129×129. a very good agreement exists for different Reynolds numbers (Re_1=100, 1000, Re_2=0) between the two numerical results is observed. Clearly, a fairly smart agreement is observed which substantiate the validity of the present code.

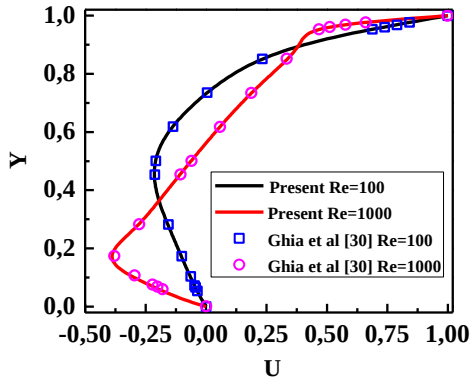

Figure 3 Code validation: U-velocity components passing through the vertical centerline for Re_1=100 and 1000 compared with results of Ghia et al [30].

6. Results and discussion

Two-dimensional steady numerical results for asymmetrical flow driving have been explored in a two-sided lid-driven square cavity with antiparallel wall motion ($U_T \neq -U_B$) for the two imposed velocity ratios, $\lambda=-7, -10$. Basically, CFD simulations are devoted to comparing the effectiveness, the reliability, and the applicability of the Laminar model against the RANS turbulent models especially the predicted secondary vortices near end walls. The laminar model will serve as a reference case. Numerical conditions that control the advantages and drawbacks of the employed models are above mentioned. The detailed analysis of the flow comparison results is presented in terms of different fluid proprieties, stream function contours, and velocity profiles.

For a comparison purpose, Figure 4 illustrates the flow configurations inside the driven cavity obtained with the laminar model at $\lambda=-10$ when the vortices are fully developed. the names of the vortices are abbreviated as follow: PV, BR, BL, TL express either primary vortex, bottom right, bottom left and top left, respectively. whereas, the numbers indicate the hierarchy of secondary vortices 1, 2, and 3 express either first, second and third, respectively. These abbreviations are generalized for all predicted flow patterns.

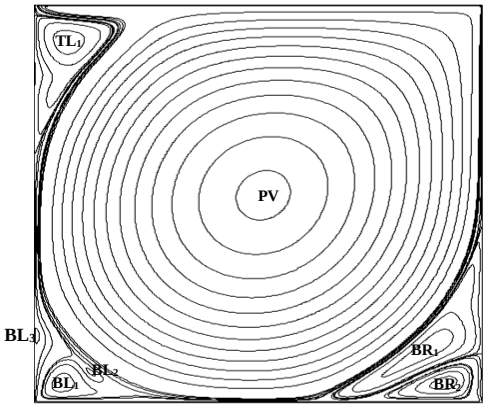

Figure 4 Flow configuration inside the cavity.

Figure 5 shows the impact of the applied Laminar model and RANS turbulence models on the flow structure inside the driven cavity in term of stream-function contours for $\lambda = -7$. In general, all performed simulations are capable to predict the same structure in the bulk of the cavity. Obviously, a discrepancy is mainly restricted to the end walls regions. The predicted computations with Laminar model, SST K-ω model, and Omega RSM model agree very well with a high ability to capture secondary vortices (PV, $BR_{1,2}$, $BL_{1,2}$, TL_1) in the near wall regions. In contrast to this, the S-A model, RNG K-ε model, and LPS-RSM model consistently show lower efficiency to capture the flow in the near wall regions. Moreover, the quantitative differences are also visible in the inability to capture the Bottom Left secondary vortices (BL_1, $BL_{2)}$. It is also seen that the performance of LPS-RSM model significantly overcomes both RNG K-ε model and S-A model.

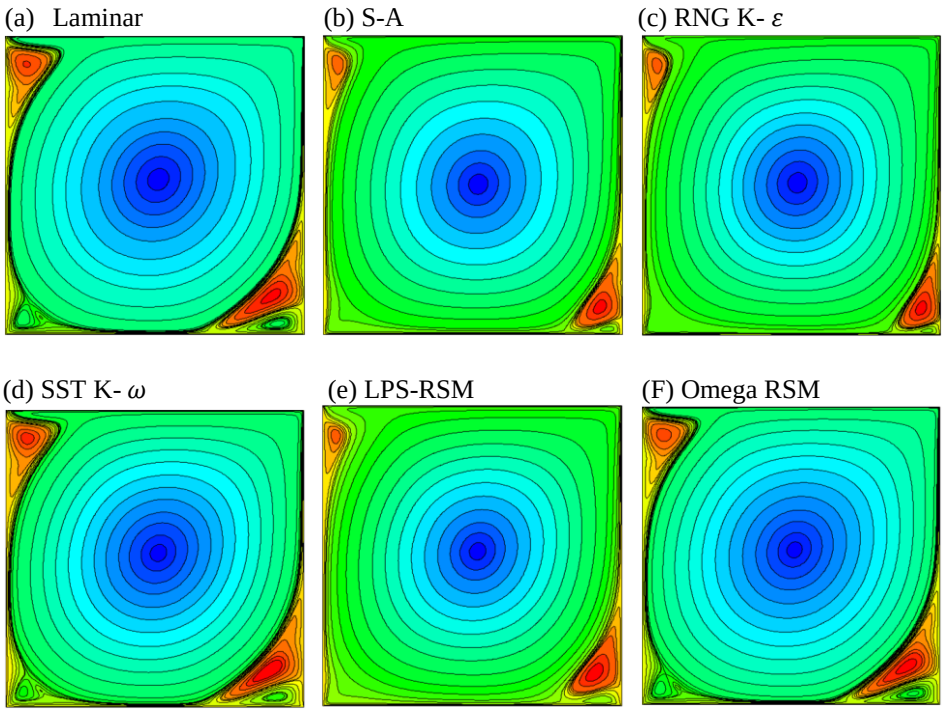

Figure 5 Stream-function contours obtained for Laminar and RANS turbulent models with $\lambda = -7$.

A further assessment of the performance evaluation of various numerical models is provided in Table 1 in terms of locations, stream-function, and vorticity values of primary and secondary vortices for $\lambda = -7$. A small difference found between the Laminar, the SST K-ω, and the Omega RSM cases with respect to stream-function and vorticity values are within acceptable limits. Evidently, results predicted with the Omega RSM model are nearly in congruence with those of the Laminar model. moreover, the maximum models' deviations in the first Bottom Right secondary vortex (BR_1) are approximately 9.8% and 8% for stream-function and vorticity values, respectively.

On the other side, results obtained from the S-A, the RNG K-ε, and the LPS-RSM cases show a significant deviation compared to the aforementioned models. They cannot adequately capture the flow near end walls which is clearly reflected on vortices properties. The maximum deviations approximately 29% and 34% respectively for stream-function and vorticity values are obtained in the first Bottom Right secondary vortex (BR_1). The deficiency of the later models is clearly demonstrated with a maximum underprediction obtained approximately of 67% and 76% respectively for stream-function and vorticity values in the BR_1 secondary vortex compared to the laminar, the SST k-ω, and the Omega RSM models. It is noteworthy that the deviation percentages are only taken in the Bottom Right

secondary vortex purposed to give insight to the overall model's efficiency near end walls as the same tendency exists on the other corners.

Table 1 Properties of primary and secondary vortices for laminar and RANS turbulent models with $\lambda=-7$.

Vortices	Fluid proprieties	Laminar	Spalart-Allmaras	RNG K-ε	SST K-ω	LPS-RSM	Omega RSM
PV	ψ	-0.121610	-7.26115E-02	-7.51070E-02	-0.11683	-0.095194	-0.12161
	ω	1.87881	1.02326	1.03432	1.78931	1.43303	1.87889
	(x, y)	0.51105, 0.52015	0.51751, 0.50371	0.51959, 0.50863	0.51104, 0.51935	0.51728, 0.51443	0.51119, 0.52016
BR_1	ψ	3.24876E-03	3.40619E-03	3.32671E-03	2.92978E-03	2.40487E-03	3.24814E-03
	ω	-2.63502	-3.59430	-3.88436	-2.42392	-2.57302	-2.62061
	(x, y)	0.89346, 0.12984	0.92481, 0.09202	0.93504, 0.08887	0.88585, 0.12416	0.90838, 0.10920	0.89320, 0.13048
BR_2	ψ	-2.33938E-03	-1.18423E-03	-9.61182E-04	-2.21676E-03	-1.25984E-03	-2.33944E-03
	ω	3.56397	6.69822	7.88488	3.72128	5.17709	3.58446
	(x, y)	0.91110, 0.03707	0.95161, 0.01856	0.95703, 0.01509	0.90599, 0.03447	0.92891, 0.01929	0.90995, 0.03667
BL_1	ψ	-2.43316E-03	-	-	-2.39586E-03	-	-2.43369E-03
	ω	2.00534	-	-	2.02444	-	2.01637
	(x, y)	0.05897, 0.05363	-	-	0.05793, 0.05176	-	0.05871, 0.05317
BL_2	ψ	-1.80753E-03	-	-	-1.82582E-03	-	-1.80764E-03
	ω	-1.14776	-	-	-0.97289	-	-1.09707
	(x, y)	0.11837, 0.0581	-	-	0.11757, 0.05456	-	0.11968, 0.0570
TL_1	ψ	2.34509E-03	9.88873E-04	1.13735E-03	2.86473E-03	6.243824E-04	2.34598E-03
	ω	-2.15074	-2.42115	-2.43228	-2.29498	-1.76969	-2.15655
	(x, y)	0.07143, 0.90603	0.04866, 0.90569	0.05017, 0.90216	0.07091, 0.90555	0.04449, 0.89992	0.07123, 0.90663

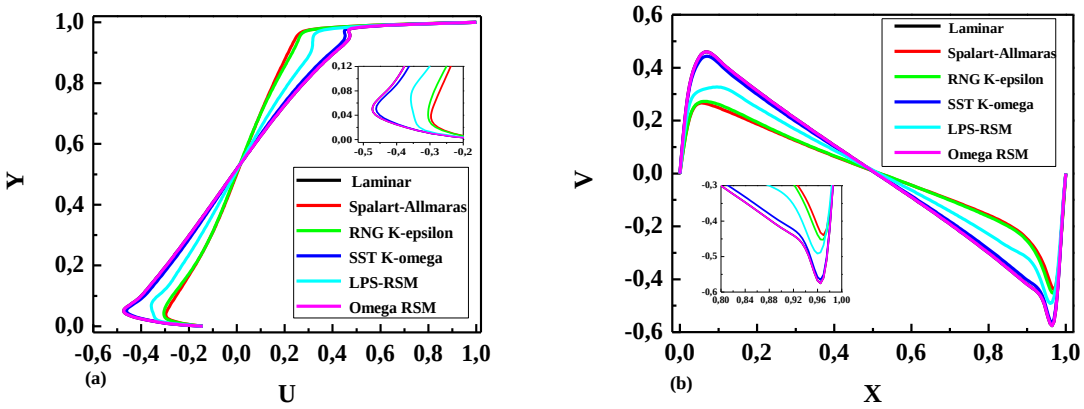

Figure 6 Comparison of velocity components profiles for Laminar and RANS turbulent models obtained with $\lambda=-7$. (a) horizontal component velocity U through the vertical centerline, (b) vertical component velocity V through the horizontal centerline.

Figure 6 (a, b) show a comparison of U- and V-velocity components profiles obtained respectively through the vertical and the horizontal centerline and calculated by the Laminar model and RANS turbulent models for $\lambda=-7$. As clearly seen, a perfect agreement exists between the obtained velocity profiles with the Laminar model and the Omega RSM model which achieve the highest velocity components peaks ($|U_{max}|$ and $|V_{max}|$) within the driven cavity, while they both indicate a close agreement with the SST K-ω model. In addition, a high discrepancy is obviously illustrated with lower velocity components peaks obtained with the LPS-RSM model, the RNG K-ε model, and S-A model. It is noteworthy that the worst performance is consistently obtained with the S-A model.

It is well known that computations in the vicinity of a relatively high Reynolds number directly influence the computational accuracy, efficiency, and stability of any CFD simulation. Therefore, in order to access an inclusive glance on the conducted comparison and elucidate the influence of the applied numerical models on the flow pattern, a higher velocity ratio which is, $\lambda = -10$ is taken into account. Figure 7 indicates a more complete picture on the impact of the applied Laminar and RANS turbulence models on the flow structure inside the driven cavity in term of stream-function contours for $\lambda = -10$. Generally, the same trend is captured by all simulations with very similar flow features. Again, all of the Laminar model; SST K-ω model; and Omega RSM model are able to provide better solutions with high sensitivity in capturing the near wall regions with an overall small difference. One additional secondary vortex namely, BL_3, is also captured in the Bottom Left corner of the cavity. On the other side, the SA model, the RNG K-ε model, and the LPS-RSM model showed a failure in mimic the dynamics of the flow. Both, the S-A and RNG K- ε simulations exhibit approximately the same flow pattern. They are able to capture the first Bottom Left secondary vortex (BL_1) compared to the examined case with $\lambda = -7$. The LPS-RSM model, however, fails to properly reflect secondary vortices on this corner and indicates an excessively underestimated flow analysis which is obvious from higher velocity component peaks ($|U_{max}|$ and $|V_{max}|$) as shown in Figure 8.

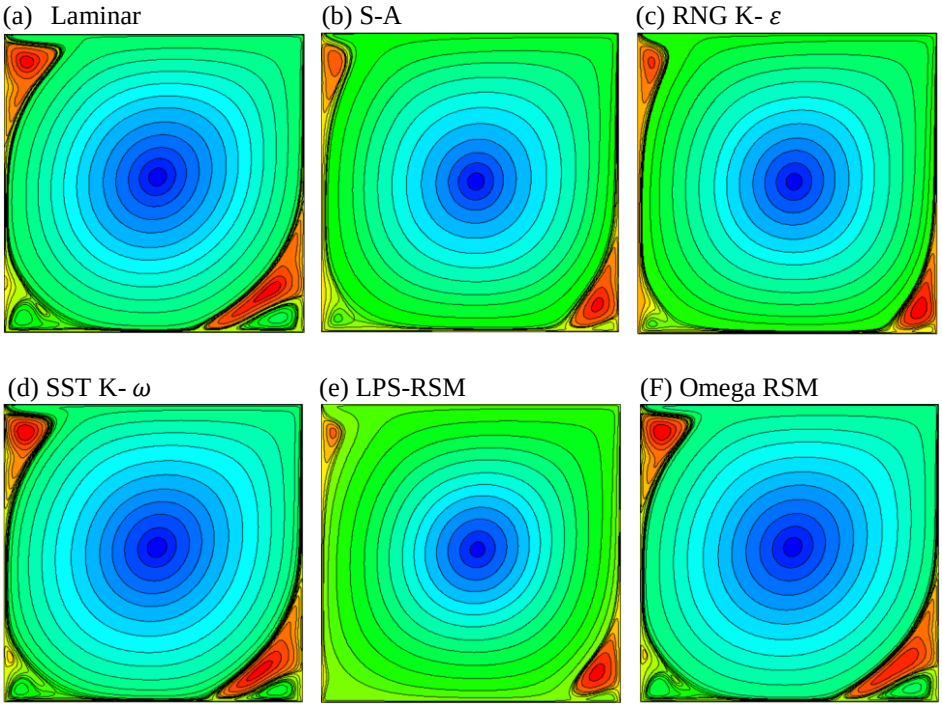

Figure 7 Stream-function contours obtained with Laminar and RANS turbulent models for $\lambda = -10$.

A more thorough examination of the conducted simulations can be accomplished by looking at the fluid properties listed in Table 2. It represents a comparison of locations, stream-function, and vorticity values in the primary and secondary vortices for laminar and RANS turbulent models displayed for $\lambda = -10$. The same picture emerges with the rising velocity ratio. Truthfully, the Laminar, the SST K-ω, and the Omega RSM cases give a fair representation of secondary vortices in the near wall regions with a relatively small overall difference. Actually, the maximum models' deviations in the first Bottom Right secondary vortex (BR_1) are approximately 10.5% and 4.5% for stream-function and vorticity values, respectively. however, fluid properties values determined by the S-A, the RNG K-ε, and the LPS-RSM simulations are not satisfactory and show a significant deviation from the aforementioned efficient

models. The maximum deviations approximately 20% and 31% respectively for stream-function and vorticity values are obtained in BR_1 the secondary vortex. Eventually, a maximum underprediction obtained approximately of 47.5% and 85.5% respectively for stream-function and vorticity values in the BR_1 secondary vortex providing better insight into the deficiency of the models compared to the laminar, the SST k-ω, and the Omega RSM models.

Table 2 Properties of primary and secondary vortices for laminar and RANS turbulent models with $\lambda=-10$.

Vortices	Fluid proprieties	Laminar	Spalart-Allmaras	RNG K-ε	SST K-ω	LPS-RSM	Omega RSM
PV	ψ	-0.12192	-6.64542E-02	-6.76449E-02	-0.10496	-8.60991E-2	-0.11315
	ω	1.88950	0.94024	0.93238	1.60447	1.29051	1.73874
	(x, y)	0.51076, 0.52173	0.52030, 0.50341	0.52215,0.50602	0.51208, 0.51874	0.52201, 0.51333	0.51118, 0.52006
BR_1	ψ	2.86189E-03	3.29176E-03	2.73338E-03	2.56654E-03	2.07912E-03	2.56225E-03
	ω	-2.64584	-3.23891	-3.57663	-2.77127	-2.46988	-2.67181
	(x, y)	0.88913, 0.14296	0.92867, 0.08991	0.94142, 0.08064	0.85613, 0.10387	0.92144, 0.09875	0.87926, 0.13217
BR_2	ψ	-2.14057E-03	-7.80443E-04	-6.00892E-04	-1.65157E-03	-7.12887E-04	-1.95583E-03
	ω	2.29379	5.47145	6.64532	2.60679	4.63490	2.26626
	(x, y)	0.91689, 0.04898	0.96074, 0.01724	0.96563, 0.013110	0.91866, 0.03766	0.94870, 0.01546	0.91463, 0.04541
BL_1	ψ	-1.77123E-03	-1.58194E-03	-1.32100E-03	-1.59142E-03	-	-1.66226E-03
	ω	1.79557	1.64554	2.29012	2.03294	-	1.89608
	(x, y)	0.06157, 0.04927	0.05549, 0.04539	0.04833, 0.03352	0.05656, 0.04249	-	0.05831, 0.04578
BL_2	ψ	-6.92086E-04	-	-	-	-	-7.09021E-04
	ω	-2.16419	-	-	-	-	-1.99416
	(x, y)	0.12543, 0.07669	-	-	-	-	0.11873, 0.07362
BL_3	ψ	1.22693E-06	-	-	7.01746E-05	-	1.97372E-05
	ω	-0.15267	-	-	-1.06820	-	-0.55856
	(x, y)	0.00741, 0.16891	-	-	0.02087, 0.15067	-	0.015125, 0.15849
TL_1	ψ	2.84766E-03	1.16347E-03	1.11274E-03	2.83932E-03	4.61942E-04	3.07739E-03
	ω	-2.24249	-2.66309	-2.44072	-2.57287	-1.59814	-2.77338
	(x, y)	0.07392, 0.90666	0.04635, 0.90547	0.04632, 0.90242	0.07095, 0.90642	0.03886, 0.90478	0.07124, 0.90683

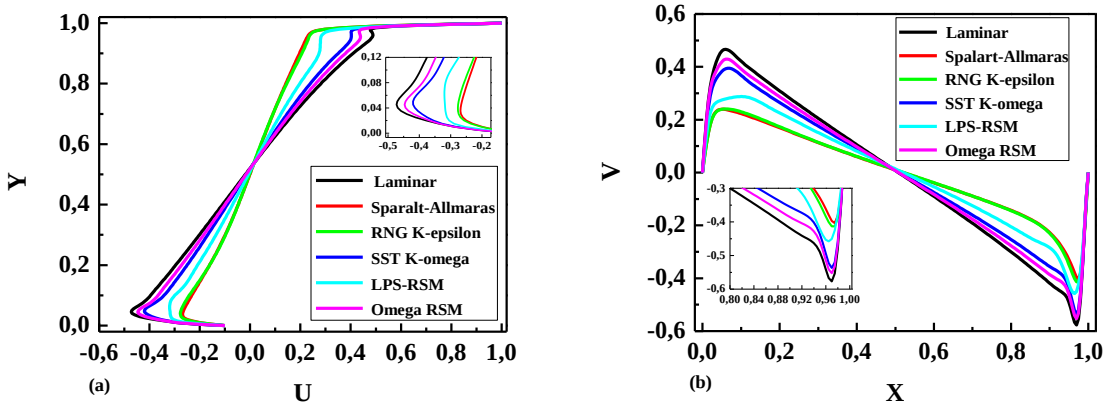

Figure 8 Comparison of velocity components profiles for Laminar and RANS turbulent models obtained for $\lambda=-10$. (a) horizontal velocity U through the vertical centerline, (b) vertical velocity V through the horizontal centerline.

Profiles of U- and V-velocity components obtained respectively through the vertical and the horizontal centerline depicted in Figure 8 provide a better comprehension into the differences between various numerical model's effect inside the driven cavity. It is clearly seen that velocity profiles determined by the Laminar model, the Omega RSM model, and the SST K-ω model are found in a small deviation and

a high ability to capture the flow in the near wall regions. It can also be seen that the Laminar model outperforms all investigated models achieving the highest velocity components peaks ($|U_{max}|$ and $|V_{max}|$) within the driven cavity. In the contrary, the results with LPS-RSM, RNG K-ε, and S-A show significant deviations and lower ability to capture the flow near end walls. In addition, the RNG K-ε model and the S-A model consistently shows lower velocity components peaks compared to LPS-RSM model while they both provide a nearly coincide velocity component profiles.

7. Conclusions

Generally, numerical computations of the fluid flow in driven cavities rely only on the Laminar model. In this investigation, steady two-dimensional flow in a two-sided lid-driven square cavity with antiparallel wall motion has been examined and compared the predictive capabilities of the Laminar model and the employed RANS turbulent models in the near wall regions. Two representative aspect ratios namely, VR=−7, −10, were considered for the inducement process when all computations were carried out with the Finite Volume Method based on the same grid. The most relevant conclusions are the followings:

1. undoubtedly, the Laminar model computations outperform the RANS turbulent models with a high ability to capture secondary vortices in the near wall regions and velocity components peaks.
2. Both, the Omega RSM model and the SST K-ω model bear approximately the same predictive features with the Laminar model with enhanced sensitivity to capture the flow in the near wall regions.
3. A discrepancy of prediction is consistently restricted to the LPS-RSM model, the RNG K-ε model, and the S-A model and clearly indicated by the flow pattern underpredictions, fluid properties deviations, and significant components velocity deviations.
4. The LPS-RSM model, however, indicates a relatively high velocity components peaks, it fails to reflect secondary vortices on the Bottom Left corner of the cavity.
5. Distinct from LPS-RSM model, almost identical predictions are found with the RNG K-ε model and the S-A model, both of which are relatively weak.
6. Finally, a better insight has been provided by this inclusive picture into the numerical model's effect in two-sided lid-driven cavity particularly and driven cavities generally.

Références

[1] H.C. Kuhlmann, M. Wanschura, and H.J. Rath, Flow in two-sided lid-driven cavities: non-uniqueness, instabilities, and cellular structures, J Fluid Mech 336 (1997) 267–299.

[2] H.C. Kuhlmann, M. Wanschura, and H.J. Rath, Elliptic instability in two-sided lid-driven cavity flow, Eur J Mech. B/Fluids 17 (1998) 561–569.

[3] S. Albensoeder, H.C. Kuhlmann, H.J. Rath, Multiplicity of steady two-dimensional flows in two-sided lid-driven cavities, J Theor Comput Fluid Dyn 14 (2001) 223–241.

[4] A. Perumal, A.K. Dass, Simulation of incompressible flows in two-sided lid– driven square cavities, Part I, FDM. CFD Lett 2(1) (2010) 13–24.

[5] A. Perumal, A.K. Dass, Simulation of incompressible flows in two-sided lid– driven square cavities, Part II. LBM. CFD Lett 2 (2010) 25–38.

[6] A. Perumal, Simulation of flow in Two-Sided Lid-Driven deep cavities by finite difference method, J Appl Sci Thermodyn Fluid Mech 6 (2012) 1–6.

[7] J.Đ. Marković, N.Lj. Lukić, J.D. Ilić, B.G. Nikolovski, M.N. Sovilj, I.M. Šijački, Using the ansys fluent for simulation of two-sided lid-driven flow in a staggered cavity, J APTEFF 43 (2012) 169-178.
[8] A. Munir, M. Riswan, M. Khan, A. Salah, Simulation of Incompressible Flow in Two Sided Lid Driven Cavity using Upwind Compact Scheme, CFD Lett. 5(3) (2013) 57-66.
[9] S. Arun, A. Satheesh, Analysis of flow behaviour in a two sided lid driven cavity using lattice Boltzmann technique, J Alexandria Eng 54 (2015) 795-806.
[10] H. Karmakar, K.S. Prandit, Numerical Solutions of Incompressible Viscous Flows in a Double-Lid-Driven Cavity, J Applied Mathematics 146 (2015) 237-243.
[11] C. Prasad, A.K. Dass, Use of an HOC scheme to determine the existence of multiple steady states in the antiparallel lid-driven flow in a two-sided square cavity, Computers and Fluids 140 (2016) 297-307.
[12] A. Perumal, Lattice Boltzmann Computation of Multiple Solutions in a DoubleSided Square and Rectangular Cavity Flows, J thermal science 6 (2018) 48-56.
[13] N. AC. Sidic, S.A. Razali, Two-Sided Lid-Driven Cavity Flow at Different Speed Ratio by Lattice Boltzmann Method, J Appl Mech Math 675 (2014) 554–679.
[14] A. Fortin, M. Jardak, J.J Gervais, R. Pierre, Localization of Hopf bifurcations in fluid flow problems, International Journal for Numerical Methods in Fluids 24 **(**1997) 1185–1210.
[15] M. Sahin, R.G. Owens, A novel fully-implicit finite volume method applied to the lid-driven cavity flow problem. Part II. Linear stability analysis, International Journal for Numerical Methods in Fluids 42 **(**2003) 79–88.
[16] F. Auteri, N. Parolini, L. Quartapelle, Numerical investigation on the stability of singular driven cavity flow, Journal of Computational Physics 183 **(**2002) 1–25.
[17] M. Poliashenko, C.K. Aidun, A direct method for computation of simple bifurcations, Journal of Computational Physics 121 **(**1995) 246–260.
[18] T. Lemée, G. Kasperski, G. Labrosse, R. Narayanan, Multiple stable solutions in the 2d symmetrical two-sided square lid-driven cavity, Comput Fluids 119 (2015) 204–212.
[19] J. O. Hinze, Turbulence. McGraw-Hill Publishing Co, New York, 1975.
[20] P.R. Spalart, S.R. Allmaras, A one-equation turbulence model for aerodynamics flows, La Recherche Aerospatiale 1 (1994) 5–21.
[21] S. A. Orszag, V. Yakhot, W. S. Flannery, F. Boysan, D. Choudhury, J. Maruzewski, and B. Patel, "Renormalization Group Modeling and Turbulence Simulations". In International Conference on Near-Wall Turbulent Flows, Tempe, Arizona, 1993.
[22] F.R. Menter, Two-equation eddy-viscosity turbulence models for engineering applications, AIAA J 32 (1994) 1598–1605.
[23] M. M. Gibson and B. E. Launder, Ground Effects on Pressure Fluctuations in the Atmospheric Boundary Layer, J. Fluid Mech 86 (1978) 491–511.
[24] B.E. Launder, Second-Moment Closure: Present... and Future?, Inter. J. Heat Fluid Flow 10(4) (1989) 282–300.
[25] B.E. Launder, G.J. Reece, and W. Rodi. Progress in the Development of a Reynolds-Stress Turbulence Closure, J. Fluid Mech. 68(3) (1975) 537–566.
[26] S. Fu, B. E. Launder, and M. A. Leschziner, "Modeling Strongly Swirling Recirculating Jet Flow with Reynolds-Stress Transport Closures, In Sixth Symposium on Turbulent Shear Flows, Toulouse, France, 1987.
[27] D.C. Wilcox, Turbulence Modeling for CFD, DCW Industries, Inc. La Canada, California, 1998.
[28] J.H. Ferziger, M. Peric´, Computational Methods for Fluid Dynamics, third, rev. ed., Springer, Berlin; New York, 2002.
[29] A. Ghobadian, S.A. Vasquez, A General Purpose Implicit Coupled Algorithm for the Solution of Eulerian Multiphase Transport Equation, International Conference on Multiphase Flow, Leipzig, Germany, 2007.
[30] U. Ghia, K.N. Ghia, C. Shin, High-Re solutions for incompressible flow using the Navier-Stokes equations and a multigrid method, J. Comput. Phys 48 (1982) 387–411.